nature communications

Article

https://doi.org/10.1038/s41467-025-66480-7

Uniform phase distribution of wide bandgap perovskite for high-performance perovskite-silicon tandem solar cells

Received: 9 September 2025

Accepted: 7 November 2025

Published online: 12 December 2025

Check for updates

Zhaoyang Han[1,2], Zhenhan Wang[1,2], Zhengchang Xia[1,2], Xingwang Zhang[1,2], Jihui Yang[3], Yuhan Liu[3], Yaxin Zhai[3], Tianyu Li[1,2], Shanshan Zhang[1,2], Lijin Wang[1,2], Qi Jiang[1,2] ✉ & Jingbi You[1,2] ✉

Metal halide perovskite-silicon tandem solar cells offer a promising pathway towards surpassing the efficiency limits of single-junction devices, and the focus remains on the wide bandgap (WBG) perovskite top cell optimization. Here, by incorporating melamine additive into a rubidium-alloyed perovskite composition, we suppress film phase separation and inhomogeneity and enhance charge carrier mobility. Consequently, our modified 1.68 eV WBG perovskite solar cells exhibit superior charge transport and minimized non-radiative recombination losses, achieving state-of-the-art performance with open circuit voltage (V_{OC}) of 1.31 V, fill factor of 86.4% and efficiency of 25%. This also derives an efficient two-terminal perovskite-silicon tandem cell with stabilized efficiency of 33.5% and high V_{OC} of 2.02 V. Both the single-junction and tandem devices show noticeable operational stability that the WBG cells maintain 80% of initial efficiency (T_{80}) after over 3200 hours of 1-sun illumination under 65°C (ISOS-L-2), while the tandem device survive T_{90} lifetime exceeding 1100 hours under the same conditions.

Crystalline silicon (c-Si) solar cells have achieved a certified photovoltaic efficiency of 27.8%, approaching the Auger-recombination-constrained Shockley-Queisser (S-Q) limit of 29.8%[1,2]. Metal halide perovskite-silicon tandem architectures, with two complementary absorption layers, provide a promising route to surpass the efficiency limit of single-junction (S-J) solar cells[3–10]. For such tandem devices, the optimal bandgap for the top perovskite cell is approximately 1.7 eV, considering the current matching with the c-Si bottom cell and maximize power output[11]. Achieving this normally requires a high bromide content in the mixed bromide-iodide (Br-I) halide perovskite composition, along with a balance of A-site cations and X-site halides in the ABX_3 structure for the desired WBG. However, the high bromide content often leads to rapid crystallization kinetics, posing challenges in obtaining uniform cation and halide distributed WBG perovskite films[3,12–15]. Consequently, spatial phase inhomogeneity could bring forth device performance losses, manifested as reduced device V_{OC}, sacrificed efficiency, and compromised operational stability, especially under light exposure combined with thermal or electrical stress[4,7,16–19].

To advance perovskite-silicon tandem technology, the primary focus remains on optimizing the WBG perovskite composition and enhancing film quality, particularly in terms of phase uniformity and purity[20,21]. Rubidium (Rb) alloying has been shown to improve the optoelectronic properties of perovskites, likely due to modified grain boundaries and inter-grain charge transport and reduced trap densities[22–24]. Additionally, Rb incorporation has demonstrated the potential for improving stability by increasing the energy barriers for ion-migration, thereby suppressing light-induced phase segregation[25–30]. However, it may also introduce new challenges related to the A-site

[1]State Key Laboratory of Semiconductor Physics and Chip Technologies, Institute of Semiconductors, Chinese Academy of Sciences, Beijing, China. [2]Center of Materials Science and Optoelectronics Engineering, University of Chinese Academy of Sciences, Beijing, China. [3]Key Laboratory of Low-Dimensional Quantum Structures and Quantum Control of Ministry of Education, Department of Physics, Hunan Normal University, Changsha, China.
✉e-mail: qjiang@semi.ac.cn; jyou@semi.ac.cn

inhomogeneity, which can lead to the formation of inactive non-perovskite secondary phases such as $RbPb(I_{1-x}Br_x)_3$, ultimately compromising both efficiency and stability. The underlying causes of these phenomena, along with strategies to achieve better phase uniformity control, remain under active investigation[22,31–33]. Therefore, it is essential to effectively harness the advantages of Rb incorporation while mitigating potential phase non-uniformity.

We develop a triple-cation RbCsFA (Cs: cesium; FA: formamidinium) WBG perovskite to replace our previously reported CsFA composition as the starting material[27]. The emergence of undesired non-active secondary Rb-rich phases prompted us to regulate the nucleation and crystallization through additive engineering. Amine groups and triazine core functionalized materials stand out as promising regulators, due to their ability to form strong electrostatic interactions through hydrogen bonding with the lead halides octahedra and A-site cations, thereby reinforcing lattice integrity and enabling defect passivation simultaneously[8,34–37]. To this end, we selected melaminium iodide (MLAI), a triazine heterocyclic compound as the regulator, which was a universal and effective additive material in some previously reported results. For example, it behaved as a good hydrogen bond acceptor and Lewis base to interact with both the organic cation and Lewis acidic lead iodide (PbI_2), which resulted in good passivation effect to the perovskite layer[35,36]. It was also adopted to construct porous and disordered PbI_2 morphology and then help convert the residual PbI_2 to perovskite phase in two-step sequential deposited perovskite films, which was based on the tridentate chelation effect between melamine and PbI_2[37].

In this work, MLAI is utilized as an effective phase uniformity regulator in our RbCsFA WBG perovskites. The strong coordination of melamine to the alloyed-cation perovskite phase can lower its formation energy and the nucleation barrier, suppressing the formation of δ-$RbPbI_3$, thus mediate homogeneous nucleation and distribution of our rubidium-containing WBG perovskite phases. The introduction of MLAI also significantly improve film and device charge transport and minimize non-radiative recombination losses. Our optimized 1.68 eV S-J WBG PSCs achieve state-of-the-art performance with a V_{OC} of 1.31 V, a FF of 86.4% and a PCE of 25%, with both V_{OC} and FF approaching 95% of their S-Q limit. The devices also exhibit excellent averaged operational stability, with T_{90} lifetime (90% of its initial efficiency) retaining for over 1400 h and T_{80} for over 3200 h under 1-sun continuous illumination at 65 °C (ISOS-L-2). Furthermore, the integrated perovskite-silicon two-terminal tandem cell reach a stabilized PCE of 33.5% (certified stabilized PCE of 32.9%), with impressive operational stability of T_{90} lifetime for over 1100 h under 1-sun at 65 °C.

Results

Perovskite phase homogeneity modulation by MLAI addition

We adopted $Rb_{0.05}Cs_{0.1}FA_{0.85}Pb(I_{0.75}Br_{0.25})_3$ (abbrev. as RbCsFA) to replace previously studied $Cs_{0.15}FA_{0.85}Pb(I_{0.77}Br_{0.23})_3$ (abbrev. as CsFA) for our WBG perovskites composition in this study[27], and the perovskite bandgap is approximately 1.68 eV (Supplementary Fig. 1). The choice was based on the potential benefits of Rb for enhancing charge carrier mobility and improving charge transport, as evidenced by transient absorption microscopy (TAM) measurements (Supplementary Note 1, Supplementary Figs. 2, 3). The RbCsFA perovskite film exhibited obviously higher carrier diffusion coefficient (D, 0.112 $cm^2 s^{-1}$) than that of CsFA (0.063 $cm^2 s^{-1}$). By using Einstein relation, the carrier mobilities (μ) were translated to be 4.43 $cm^2 V^{-1} s^{-1}$ and 2.43 $cm^2 V^{-1} s^{-1}$ for RbCsFA and CsFA, respectively. These improvements showed the great potential of RbCsFA for better charge transport and solar cells applications. Initial solar cells fabrication also demonstrated significant advances in reducing device hysteresis and overall efficiencies, further validating the promises of RbCsFA perovskite and setting a good benchmark for further study (Supplementary Fig. 4).

Although RbCsFA composition is a potential perovskite absorber for further solar cells application, we found there were phase segregation existed in the original perovskite film. As shown in Fig. 1a, from the top view scanning electron microscopy (SEM) analyses, crystallized flake-like secondary phase precipitation was observed on the top surface. Energy dispersive X-ray spectroscopy (EDS) analyses revealed that these were aggregated Rb-rich species (Supplementary Fig. 5). Grazing incidence X-ray diffraction (GIXRD) further confirmed that these were non-perovskite δ-$RbPbX_3$ (X denotes the combinations of I and Br halide), indicated by a characteristic (110) diffraction peak at 10.18° and comparison with a powder diffraction file (PDF) of δ-$RbPbI_3$[38] (Fig. 1b). Here we used $RbPbI_3$ as a reference considering the undistinguishable XRD patterns of $RbPbI_3$ and $RbPbBr_3$[39,40]. As for depth-dependent distribution by GIXRD, the intensity ratio of the (110) peak of δ-$RbPbI_3$ to the perovskite (100) peak (14.14°) decreased from 12.3 to 6.1% as the incident angle increased from 0.5° to 2.0° (Fig. 1c, Supplementary Fig. 6a). The tilt cross-sectional SEM image also visualized that the main accumulation of δ-$RbPbI_3$ was located at the perovskite top surface (Supplementary Fig. 6b). The preferential precipitation of δ-$RbPbI_3$ on the top surface can be attributed to the top-to-down crystallization during annealing, coupled with the lower formation energy of δ-$RbPbI_3$ phase, for which we will discuss later[16,41,42]. To fully exploit the advantages of Rb-containing WBG perovskites and mitigate non-uniform phase distribution, we introduced MLAI into the perovskite. Surface SEM image and GIXRD results confirmed the absence of the δ-$RbPbI_3$ phases on the MLAI-modified perovskite film (Fig. 1d, e, Supplementary Fig. 7). EDS analyses further validated the disappearance of Rb-rich phase and a uniform Rb distribution (Supplementary Fig. 8).

We conducted density functional theory (DFT) calculations to reveal the phase formation process of the perovskite films. The formation energy calculations revealed that the thermodynamic formation energy of δ-$RbPbI_3$ and alloyed cation phase of α-$RbFACsPbI_3$ are −3.42 eV/unit and −3.21 eV/unit, respectively, before melamine addition (Fig. 1f). The calculation details can be found in Supplementary Note 2 and Supplementary Fig. 9. The nucleation barriers calculations revealed that the nucleation barriers (ΔG^*) for δ-$RbPbI_3$ and α-$RbFACsPbI_3$ are 0.28 eV and 0.42 eV, respectively (Supplementary Note 3, Fig. 1g). Since the formation energy and nucleation barrier of δ-$RbPbI_3$ are both lower compared with that of alloyed cation phase, δ-$RbPbI_3$ is more likely to nucleate first and then precipitated at perovskite top surface during the crystallization process, which was consistent with GIXRD and EDS results. After introducing melamine, the formation energy of α-$RbFACsPbI_3$ (−3.76 eV/unit) can be reduced to even below that of δ-$RbPbI_3$ (−3.62 eV/unit) (Fig. 1f). Moreover, the introduction of melamine also significantly lowers the nucleation barrier ΔG^* for the alloyed cation phase (0.12 eV), compared with δ-$RbPbI_3$ (0.15 eV) (Fig. 1g). This finally enhanced the nucleation rate of alloyed cation phase according to the Arrhenius-type formula (Supplementary Eq. 8), which significantly promoted the preferred nucleation of α-$RbFACsPbI_3$, thereby inhibiting the precipitation of δ-$RbPbI_3$ (Supplementary Note 3). Through X-ray photoelectron spectroscopy (XPS) analysis, clear peak shifts of the Rb 3*d*, Pb 4*f*, Cs 3*d* and N 1*s* toward higher binding energies was observed, which means that the Fermi level is more distant to the core level, indicating that there was strong interaction between melamine with lead halides octahedra and A-site cations. And the strong interaction should be responsible for the formation energy changes (Supplementary Fig. 10). Note that a weak signal corresponding to the metallic Pb^0 state—identified by the Pb $4f_{7/2}$ and Pb $4f_{5/2}$ peaks located at around 136.06 eV and 140.89 eV, respectively, was detected in the control sample but disappeared in target sample. We attribute this signal to the reduction of PbI_2 induced by high-energy X-ray exposure during the XPS measurement, where the PbI_2 diffraction peak was also detected in the XRD patterns of

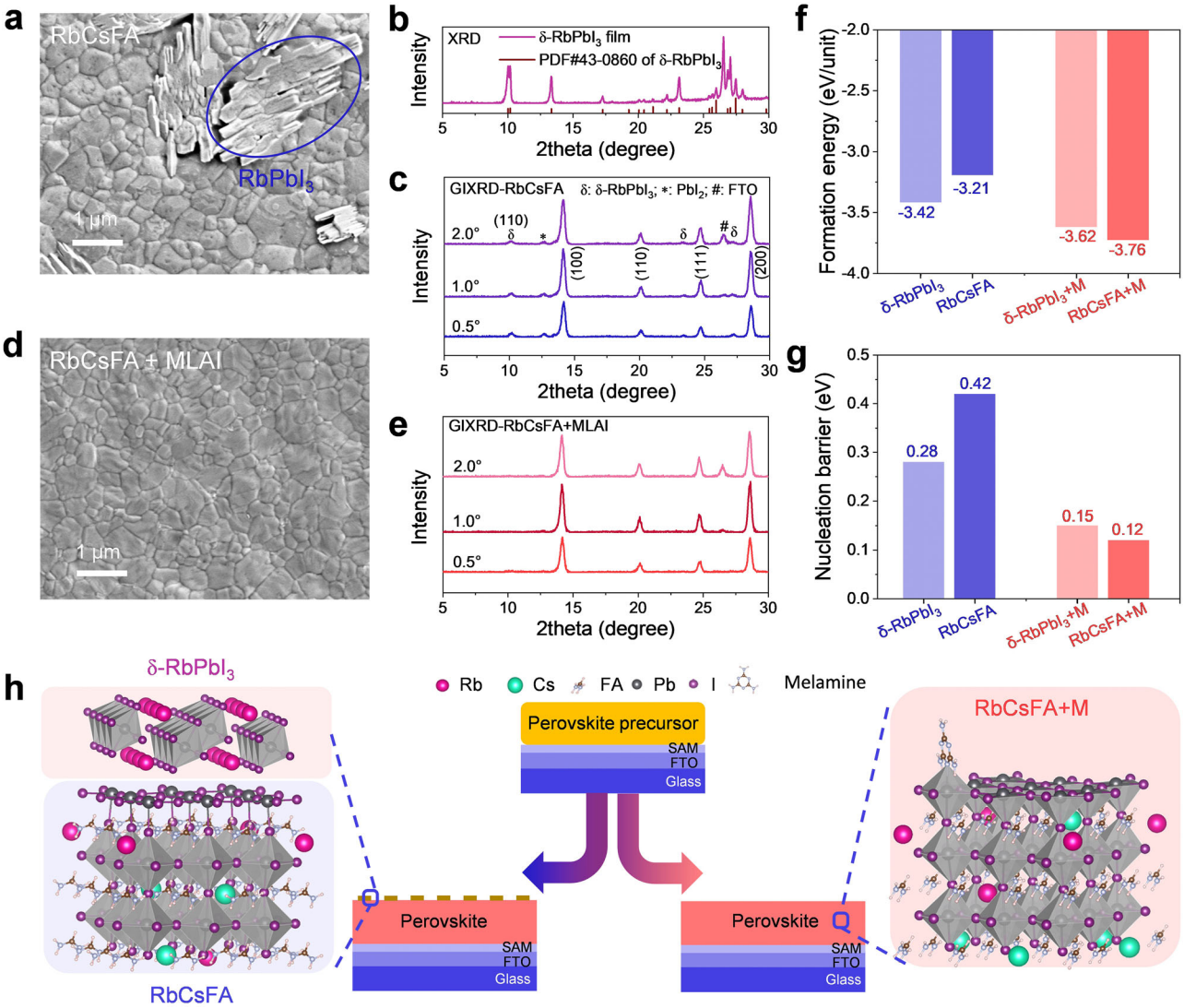

Fig. 1 | Perovskite composition and phase uniformity modulation. a Scanning electron microscopy (SEM) surface image of $Rb_{0.05}Cs_{0.1}FA_{0.85}Pb(I_{0.75}Br_{0.25})_3$ (abbrev. as RbCsFA) perovskite film, the marked aggregated material was confirmed to be $RbPbI_3$ by energy dispersive X-ray spectroscopy (EDS) analysis in Supplementary Fig. 5 and grazing incident X-ray diffraction (GIXRD) results in (**c**). **b** XRD/Powder diffraction file (PDF) card information of $RbPbI_3$. **c** GIXRD patterns of RbCsFA perovskite film at different incident angles. **d** SEM surface image of RbCsFA with melaminium iodide (MLAI) additive. **e** GIXRD patterns of RbCsFA perovskite film with MLAI at different incident angles. **f**, **g** Formation energy and nucleation barriers of δ-$RbPbI_3$ and RbCsFA perovskite with and without melamine (denote M in the graphs, calculated by density functional theory (DFT) calculations. **h** Schematic diagram of the perovskite film formation comparison with and without melamine. SAM self-assembled monolayers, FTO fluorine-doped tin oxide.

control perovskite film (Fig. 1c). And we could also expect that the target perovskite phase possesses superior stability under high-energy X-ray irradiation compare to the control sample, thereby mitigating such reduction effects.

A schematic diagram of perovskite film formation comparison was depicted in Fig. 1h. The melamine addition function as a crystallization regulator to the Rb-containing composition, promote the uniform alloy-cation phase distribution in the final perovskite film and suppress the δ-$RbPbI_3$ non-perovskite phase precipitation.

There is optimal MLAI additive concentration window for suppressing δ-$RbPbI_3$, as demonstrated by the SEM surface morphologies in Supplementary Fig. 11, where the target concentration is around 4 mM with the most uniform phase distribution. At lower MLAI concentration, the suppression of δ-$RbPbI_3$ precipitation was incomplete, while higher concentration could hinder grain growth, reduce the perovskite grain size and potentially create transport barriers at grain boundaries. By comparing device efficiencies and photovoltaic parameters across different MLAI concentrations, we also determined 4 mM to be the target concentration for further optoelectronic investigations (Supplementary Fig. 12).

To gain deeper insights into the perovskite film growth mechanism, we performed in-situ photoluminescence (PL) spectrometry monitoring during the film formation process. As shown in Fig. 2a, b, the target perovskite film with 4 mM MLAI addition exhibited a noticeable slower PL peak shift and a more gradual intensity change during the initial crystallization stage (0–2 s), compared to the control film without MLAI. These observations suggested that MLAI effectively retards the crystallization process, which is expected to facilitate the formation of high-quality WBG perovskite films with improved phase homogeneity[43,44].

We also conducted TAM to evaluate the bulk charge transport properties of perovskite film with or without MLAI. The target film exhibited an enhanced carrier diffusion coefficient (0.147 $cm^2 s^{-1}$) and carrier mobility (5.69 $cm^2 V^{-1} s^{-1}$) than that of the control film (D of 0.112 $cm^2 s^{-1}$ and μ of 4.43 $cm^2 V^{-1} s^{-1}$) (Supplementary Note 1, Supplementary Figs. 2, 3), suggesting that the perovskite films charge

https://doi.org/10.1038/s41467-025-66480-7

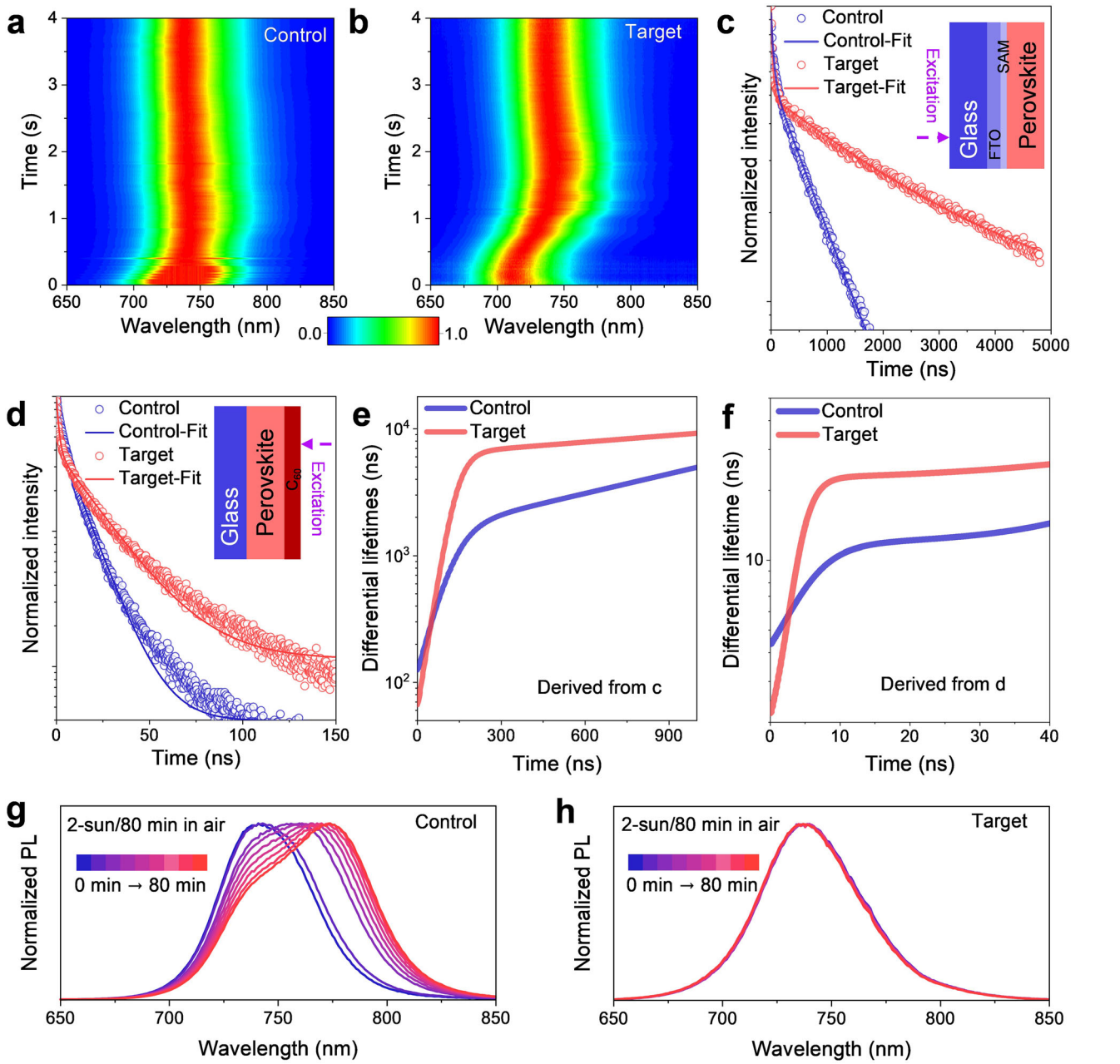

Fig. 2 | Perovskite film optoelectronic properties and comparisons. a, **b** In-situ photoluminescence (PL) monitoring during the perovskite film growth of the initial annealing process. **c** Time-resolved photoluminescence (TRPL) decay curves with the sample stack of glass/FTO/CbzNaph/perovskite, where CbzNaph is hole-selective self-assembled molecule of (4-(7H-dibenzo[c,g]carbazol-7-yl)butyl)phosphonic acid. The laser pulse fluence is around 4 nJ cm^{-2}. **d** TRPL decay curves comparisons with the sample stack of glass/perovskite/modification layer/C_{60}, where the modification layer was a mixture of ethylenediammonium diiodide ($EDAI_2$) and phenethylammonium iodide (PEAI) in this study. **e**, **f** The differential lifetime derived from **c**, **d**, respectively. **g**, **h** In-situ time-dependent PL evolutions for control and target perovskite films under 2-sun intensity illumination for 80 min in ambient air. The sample stack is glass/FTO/CbzNaph/perovskite.

transport was further enhanced after MLAI regulation. In parallel, time-resolved photoluminescence (TRPL) measurements were conducted on two device configurations (as illustrated in the inserts of Fig. 2c and d). For the stack of glass/FTO/CbzNaph/perovskite, bi-exponential fitting of the decay curves yielded an average carrier lifetime of 2.47 µs for the target sample, significantly longer than the 0.8 µs observed for the control (Fig. 2c, Supplementary Table 1). This result suggests a notable reduction in defect density and suppression of non-radiative recombination in target perovskite film. Similar improvement was also observed for the stack of glass/FTO/perovskite/$EDAI_2$ + PEAI/C_{60} (Fig. 2d, Supplementary Table 2). To further investigate interfacial charge dynamics, we performed differential lifetime ($\tau_{PL}(t)$ analysis based on the TRPL data by computing the inverse negative slope of the logarithmically plotted PL photon flux $\phi(t)$. From the differential lifetime graph (Fig. 2e, f), the first interval at shorter times of the steep rise represents the charge extraction/transfer process and the sharpness of the rise implies the speed of the charge transfer, the transition from the ascending trend to a plateau signals the cessation of charge transfer, after which the second interval at longer delay times represents the non-radiative recombination dominant process[45,46]. In both configurations, the target samples exhibited a sharper rise in the initial time region, indicating more efficient charge transfer and reduced

https://doi.org/10.1038/s41467-025-66480-7

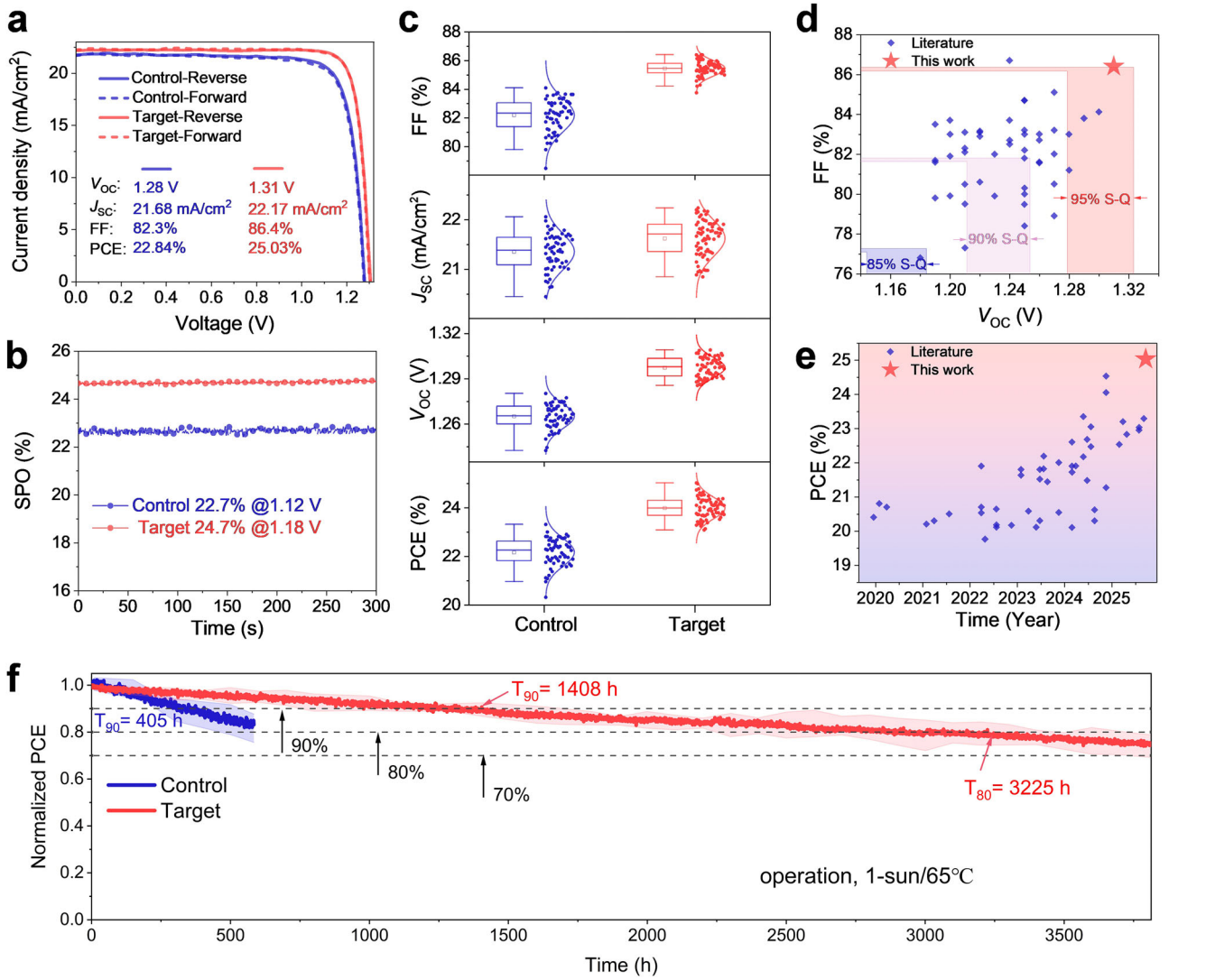

Fig. 3 | Single junction WBG PSCs efficiency and stability performance. **a** Representative *J*–*V* curves comparison of control and target PSCs. **b** Stabilized power output (SPO) efficiencies, tracked at the maximum power point. **c** Device statistical photovoltaic parameters (PCE, V_{OC}, J_{SC} and FF). The box plots illustrate the mean, median line, 25–75% box limits with 1.5× interquartile range whisker. **d**, **e** Comparison plots of the V_{OC}, FF and PCE for WBG (1.64–1.69 eV) single-junction PSCs, derived from Supplementary Table 4. The colored regions in (**d**) represent V_{OC} and FF values corresponding to 95%, 90%, and 85% of their S-Q limit, the left and right boundaries of these regions correspond to bandgaps of 1.64 eV and 1.69 eV, respectively. **f** Operational stability of encapsulated devices under continuous 1-sun illumination at 65 °C. The devices were placed in a tightly closed chamber in air and nitrogen (N_2) flow was maintained in the chamber during the testing. A temperature sensor inside the chamber was used to ensure the chamber temperature of 65 °C. We used 6 individual devices for each stability test to obtain the average degradation behavior, with the error bars representing the standard deviations. The initial efficiencies were around 20–21.5% and 23.5–24% for control and target devices (without antireflection layer), respectively, when measured at room temperature.

trap-assisted recombination at both SAM/perovskite and perovskite/C_{60} interfaces, compared to control[47,48]. The mitigated aggregation of δ-$RbPbI_3$ phase and homogeneous phase distribution greatly helped bulk and interfacial charge transfer properties.

We further evaluated the photostability of the films by conducting in-situ time-dependent PL measurements under continuous illumination. As shown in Fig. 2g, h, the PL emission peak of the control sample red-shifted by approximately 35 nm after 80 min exposure of 2-sun intensity in air, indicating severe photoinduced phase segregation. In contrast, the MLAI-modified perovskite film exhibited negligible peak shift, underscoring its improved photostability and effective suppression of phase segregation and ion migration. These results suggested that MLAI-incorporated perovskite films hold great potential for better solar cell applications.

Single junction WBG photovoltaic performance and analysis

To comprehensively evaluate the effectiveness of WBG S-J PSCs after introducing MLAI into perovskite film, we fabricated devices with the configuration of glass/FTO/CbzNaph/$Rb_{0.05}Cs_{0.1}FA_{0.85}Pb(I_{0.75}Br_{0.25})_3$/$EDAI_2$ + PEAI/C_{60}/SnO_2/Cu. As shown in Fig. 3a, the representative current density-voltage (*J*–*V*) curves based on MLAI-optimized devices delivered a state-of-the-art efficiency of 25.03%, featuring a V_{OC} of 1.31 V, FF of 86.4%, and J_{SC} of 22.17 mA/cm² under reverse scan direction, without hysteresis. In contrast, the control device obtained a reverse scan efficiency of 22.84% (V_{OC} of 1.28 V, J_{SC} of 21.68 mA/cm², and FF of 82.3%) (Supplementary Table 3). Note that we also fabricated devices without the surface treatment to evaluate the V_{OC} improvement resulting from MLAI addition. As shown in Supplementary Fig. 13, the V_{OC} also increased approximately 0.04 V (from 1.24 V without MLAI

to 1.28 V with MLAI). The enhancement is consistent with that observed in devices treated with $EDAI_2$ and PEAI. The additional surface treatment contributed a further V_{OC} increase of 0.03 V. What's more, MLAI couldn't act as an effective surface passivation material in our perovskite system (Supplementary Fig. 13). The corresponding stabilized power output (SPO) efficiency under their maximum power point was increased from 22.7% for control to 24.7% for target, respectively (Fig. 3b). The integrated J_{SC} from the external quantum efficiency (EQE) are 21.37 mA/cm^2 and 21.53 mA/cm^2 for control and target devices, respectively, which aligned well with the *J*–*V* characteristics (Supplementary Fig. 14). The determined bandgaps both were approximately 1.68 eV from the first derivative of the EQE spectra, and the incorporation of MLAI didn't change the perovskite bandgap. Our device efficiency was independently certified at National Photovoltaic Industry Measurement and Testing center (NPVM), where the reverse scan efficiency was 24.92%, with a V_{OC} of 1.31 V, a J_{SC} of 22.15 mA/cm^2, and an FF of 86.15%. The forward scan efficiency was 24.83%, with a V_{OC} of 1.31 V, a J_{SC} of 22.15 mA/cm^2, and an FF of 85.81%, along with the stabilized efficiency of 24.08% after 300 s maximum power point tracking (Supplementary Fig. 15). These results aligned closely with our laboratory measurements.

To assess the repeatability of the MLAI modification, we collected photovoltaic parameters from 60 control devices and 73 target devices for the statistical distributions analysis. The average device efficiency increased from 22.2 to 24%, alongside narrower parameters distributions for the target devices (Fig. 3c). The superior efficiencies with the obvious V_{OC} and FF increasement, can be attributed to the superior bulk perovskite quality and improved interfacial charge transfer thanks to MLAI modification. The delayed crystallization helped providing a larger process window to achieve excellent device reproducibility and reliability.

We further compared our WBG PSCs results with previously reported devices (1.64–1.69 eV bandgaps), as summarized in Supplementary Table 4 and we derived the visualized results as Fig. 3d, e. For this bandgap range, three ranges were defined for V_{OC} and FF as 95%, 90%, and 85% of the S-Q limit. Our results way exceeded literature values, achieving 95% of the S-Q limit for both the V_{OC} and FF. Moreover, our best PCE of 25% also way beyond the reported PCEs across 1.64–1.69 eV bandgaps and surpassed 85% of its S-Q limit (Fig. 3e), demonstrating our great endeavor and progress in pushing forward the thermodynamic potential of the WBG perovskite absorbers.

To gain deeper insights into the improved device efficiencies, we investigated the carrier recombination and charge transport behaviors, by recording the device *J*–*V* responses under varied light intensities (Supplementary Fig. 16). Both the control and MLAI modified devices displayed a linear relationship of J_{SC} versus light intensity with the slope close to 1, indicating that the bimolecular recombination is negligible and implied the unimpeded carrier transport and collecting within the solar cells[49,50]. For the linear relationship of V_{OC} with the natural logarithmic of light intensity, where the slope of the plots can determine the ideality factor (*n*), the target device delivers an *n* value of 1.08, much lower than that of the control device of 1.21, suggesting a substantial attenuation of defect-assisted recombination in target device[51,52]. Electroluminescence (EL)-EQE further supported these findings (Supplementary Fig. 17). At an injection current density of 22.14 mA/cm^2, an EL efficiency (EQE_{EL}) of the target device reached 12.6%, whereas only 1.1% for the control. Based on EL-EQE results, the V_{OC} non-radiative recombination loss $\Delta V_{oc}^{non-rad}$ of control and target device were calculated to be 0.12 V and 0.06 V according to Supplementary Eq. 13, aligning well with the *J*–*V* results (Supplementary Note 4)[53,54]. The greatly enhanced EL efficiency and minimal $\Delta V_{oc}^{non-rad}$ confirmed the improved optoelectronic quality of perovskite and the suppressed non-radiative recombination in the entire device after MLAI addition. Dark *I*–*V* characteristics showed that the target device exhibited higher shunt resistance, reduced series resistance and lower leakage current compare to control, also suggesting more efficient overall charge transport and suppressed non-radiative recombination losses[55,56] (Supplementary Fig. 18).

To assess device stability, we tracked the encapsulated devices operational stability under 1-sun light-emitting diode (LED) illumination at 65 °C. The MLAI-incorporated device retained 90% of its initial PCE (T_{90}) after over 1400 h and kept T_{80} lifetime for over 3200 h, with 6 averaged device results (Fig. 3f). Note that one champion device survived over 3800 h of T_{80} lifetime (Supplementary Fig. 19), and our stability results substantially surpassed the current literature reports for WBG (~1.68 eV) PSCs (Supplementary Table 5). In stark contrast, the control devices exhibited averaged T_{90} lifetime for only 405 h. For the detail degradation comparison of each of the solar cell parameters including *V*oc, FF and J_{SC}, all of them decayed faster for the control sample, indicating that both the perovskite bulk and device interfaces possibly underwent more severe degradation under light and heat combination (Supplementary Fig. 19). The spectrum of the LED light source for stability measurement was depicted in Supplementary Fig. 20. We also conducted thermal stability tests under 85 °C, five control and ten target devices were monitored that they showed similar trends without obvious efficiency drop (Supplementary Fig. 21), indicating that light soaking is a harsher condition for phase segregation in our perovskite system. The greatly improved operational stability under elevated temperature and light-soaking could be attributed to the homogenized phase distribution, improved perovskite crystallization quality, facilitated charge transport, and suppressed phase segregation.

Perovskite-silicon tandem device performance and analysis

To further check the active role of our additive strategy for WBG perovskites, we applied our optimized WBG perovskite atop of a double-textured silicon heterojunction solar cell (SHJ). A schematic stack of the silicon-perovskite two-terminal tandem structure is depicted in Fig. 4a. Before integrating with silicon cell, 1 cm^2 semitransparent single-junction WBG PSCs was fabricated to check the uniformity of perovskite film and effectiveness of MLAI regulation with the structure of ITO/CbzNaph/perovskite/$EDAI_2$ + PEAI/C_{60}/SnO_2/indium zinc oxide (IZO)/silver (Ag) grid. Upon illumination from the IZO side, the MLAI modified device delivered the best PCE of 22.77%, with a J_{SC} of 21.07 mA/cm^2, V_{OC} of 1.29 V, and FF of 83.48%, while the control exhibited inferior PCE of 20.51%, with a J_{SC} of 20.59 mA/cm^2, V_{OC} of 1.25 V, and FF of 79.4% (Fig. 4b and Supplementary Fig. 22a). The EQE spectra of the corresponding devices were shown in Supplementary Fig. 22b, where the integrated J_{SC} of 20.81 mA/cm^2 and 20.36 mA/cm^2 for target and control device, respectively, also aligned well with their *J*–*V* characteristics. The obviously enhanced J_{SC} of the target device should be attributed to the better perovskite/C_{60} interface quality after involving MLAI to mitigate the aggregated Rb-rich phase on top of perovskite surface and achieve uniform phase distribution. A cross-sectional SEM image showed the high-quality deposition of the perovskite film on the textured silicon substrate (Supplementary Fig. 23). The *J*–*V* characteristics of our representative tandem device, shown in Fig. 4c, yielded a PCE of 33.91%, with a V_{OC} of 2.02 V, J_{SC} of 20.22 mA/cm^2, and FF of 83.15% under reverse scan, and a PCE of 34.02%, V_{OC} of 2.02 V, J_{SC} of 20.23 mA/cm^2, and FF of 83.38% under forward scan, along with the SPO efficiency delivering 33.5% (Fig. 4d). The insert shows a photo of the tandem device. The J_{SC} values derived from the integration of the top WBG subcell and the bottom silicon subcell EQE tests were 20.1 mA/cm^2 and 19.9 mA/cm^2, respectively (Fig. 4e), which closely match the J_{SC} values obtained from the *J*–*V* measurements. Compared to reported literature values, our V_{OC}×FF product and PCE are among the same level of highest reported values, especially that our impressive V_{OC} of 2.02 V is

https://doi.org/10.1038/s41467-025-66480-7

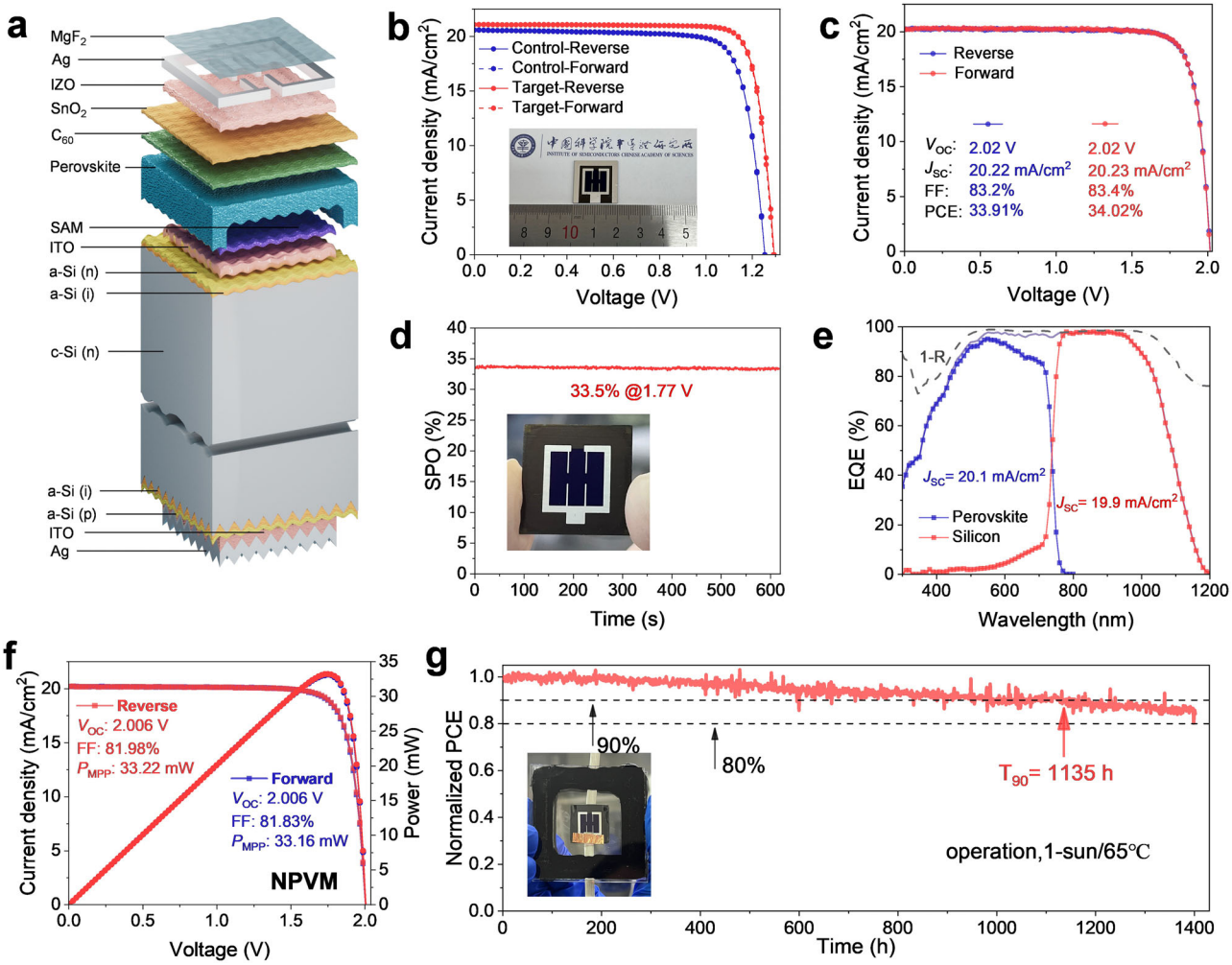

Fig. 4 | 1 cm² semi-transparent single junction and perovskite-silicon tandem solar cells performance. a The schematic device structure of silicon/perovskite tandem solar cells. **b** *J*–*V* curves of 1 cm² semitransparent S-J WBG PSCs with and without MLAI. The inset shows the device image. **c** *J*–*V* curves of our representative silicon/perovskite tandem solar cell. **d** The corresponding SPO of the silicon/perovskite tandem cell. The inset shows the tandem device photo. **e** EQE spectra of the corresponding silicon/perovskite tandem device. **f** *J*–*V* and power-voltage curves of the silicon/perovskite tandem device measured by NPVM. **g** Packaged tandem device operational stability under 1-sun illumination at 65 °C in air, the insert shows the packaged tandem cell image.

the highest value ever reported, affirming the success of our MLAI-modified WBG perovskites in reducing the energy loss and advancing tandem solar cells efficiency (Supplementary Fig. 24, Supplementary Table 6). The tandem device efficiency was also independently measured in NPVM certification center. It showed a certified PCE of 33.22%, with a V_{OC} of 2.01 V, J_{SC} of 20.2 mA/cm², and FF of 81.98% under reverse scan; PCE of 33.16%, V_{OC} of 2.01 V, J_{SC} of 20.2 mA/cm², and FF of 81.83% under forward scan, along with a certified stabilized efficiency of 32.85% after MPP tracking for 300 s (Fig. 4f and Supplementary Fig. 25). In addition, our tandem cell exhibited excellent operational stability, with encapsulated devices maintaining a T_{90} lifetime for 1135 h under 1-sun/65 °C (ISOS-L-2) (Fig. 4g). While the results are promising, the efficiency parameters of our as-used silicon bottom cells are far below the world's most advanced level (Supplementary Fig. 26), which limited the final tandem device efficiencies in this study. Note that we achieved high FF of 83% for the tandem cell, indicating that the limitations observed in the standalone bottom cell—whether resistive or related to defects—are effectively compensated within the integrated, current-matched tandem stack[57,58]. There is still much room for the further optimization and advancement. Apart from silicon bottom cell optimization, future work could focus on optimizing the functional layers of the semitransparent conductive electrodes such as IZO, electron transport layers of C_{60} and SnO_2, to improve transmission and minimize parasitic absorption, thereby increasing the current of the overall tandem device.

Discussion

We demonstrated our Rb-alloyed WBG perovskites suffered from uneven phase distribution and aggregated δ-$RbPbI_3$ phase on top of the perovskite surface, which remained an obstacle towards enhancing device charge transport and transfer, minimizing non-radiative recombination losses and improving device operational stability. By incorporating MLAI additive in the WBG perovskite film, the δ-$RbPbI_3$ phase precipitation was greatly suppressed and the homogeneous alloy-cation phase was more preferred to be formed. This significantly elevated the perovskite film quality, mitigated phase segregation and enhanced the device charge extraction, resulted in simultaneously enhanced solar cells efficiency and stability performance. Our additive engineering strategy could establish a feasible pathway toward highly efficient and stable perovskite-silicon solar cells, and bring confidence for more future breakthroughs.

Methods

Materials

Dimethylformamide (DMF), dimethyl sulfoxide (DMSO), chlorobenzene (CB), isopropanol (IPA), ethanediamine dihydroiodide ($EDAI_2$), ethyl acetate (EA), lead iodide (PbI_2), melamine and hydriodic acid were purchased from Sigma Aldrich. cesium iodide (CsI), formamidinium iodide (FAI), phenethylammonium iodide (PEAI), lead bromide ($PbBr_2$), (4-(7H-dibenzo[c,g]carbazol-7-yl)butyl)phosphonic acid (CbzNaph) were purchased from Xi'an Yuri Solar Company Limited. C_{60} was purchased from Luminescence Technology. All the chemicals are used directly without further purification. The synthesize of melaminium iodide (MLAI):1 g of melamine powder (99% purity, Sigma-Aldrich) was combined with 2 mL of hydroiodic acid (57% weight in water, Sigma-Aldrich) and 25 mL of methanol in a 50 mL three-neck round-bottom flask under a nitrogen atmosphere for 12 h with stirring. The resulting suspension was transferred to a centrifuge tube, and the white precipitate was separated from the solution via centrifugation. Subsequently, the precipitate was sequentially washed with methanol, ethanol, diethyl ether, and then placed in a vacuum oven to dry at 65 °C for 12 h.

Preparation of precursor solutions

The $Rb_{0.05}Cs_{0.1}FA_{0.85}Pb(I_{0.75}Br_{0.25})_3$ perovskite precursor (1.75 M), was prepared by dissolving a mixture of PbI_2 (504.2 mg), $PbBr_2$ (240.8 mg), FAI (255.9 mg), CsI (45.5 mg), and RbI (18.6 mg) in a mixture solvent of DMF and DMSO (1 mL, v:v = 4:1). For the target perovskite precursor solution, melaminium iodide (MLAI) (4 mM, ~1 mg mL^{-1}) was directly added into the precursor, and the precursor was stirred at room temperature in a N_2 glove box for 4 h. The self-assemble hole selective molecule (SAM) solution was prepared by dissolving CbzNaph in ethanol solvent with the concentration of 1 mg mL^{-1}.

Single-junction perovskite solar cells device fabrication

The device structure is: Glass/FTO/CbzNaph/Perovskite/$EDAI_2$ + PEAI/C_{60}/SnO_2/Cu. $Rb_{0.05}Cs_{0.1}FA_{0.85}Pb(I_{0.75}Br_{0.25})_3$ was used as the perovskite composition. FTO glass was cleaned using detergent, deionized water, acetone and IPA before drying in a N_2 flow. Next, the FTO substrate was treated by ultraviolet ozone for 15 min and then transferred to N_2 glove box. 1 mg mL^{-1} CbzNaph solution was deposited on the FTO at 3000 r.p.m. for 30 s, and annealed at 100 °C for 10 min. For the perovskite layer deposition, 1.75 M perovskite precursor solution was deposited on the FTO/SAM substrate at 2500 r.p.m. for 40 s with the accelerated speed of 700 r.p.m./s. Then the obtained perovskite precursor wet film was put on a low temperature (e.g., 20 °C) substrate and moved to a vacuum chamber, and pumped down to around 20 Pa for 60 s. After that, the films were annealed at 100 °C for 20 min. After that, 1 mg mL^{-1} $EDAI_2$ and 1 mg mL^{-1} PEAI mixture solution in IPA was coated on the perovskite surface at 4000 r.p.m. for 20 s and annealed at 100 °C for 5 min. 20 nm C_{60}, 15 nm tin oxide (SnO_2) were finished by thermally evaporation and atomic layer deposition, respectively. Finally, 150 nm Cu (2.0 Å s^{-1}) was thermally evaporated as the electrode using a shadow mask. The device area was 0.108 cm^2, and a 0.0725 cm^2 non-reflective mask was used to define the accurate active cell area when conducting *J*–*V* measurements. For 1 cm^2 semi-transparent single-junction device, the device stack is ITO/CbzNaph/perovskite/$EDAI_2$ + PEAI/C_{60}/SnO_2/indium zinc oxide (IZO)/silver (Ag) grid. The thicknesses of C_{60}, SnO_2, and IZO were 15 nm, 15 nm, and 40 nm, respectively.

Perovskite-silicon tandem solar cells fabrication

Our silicon bottom cell was silicon heterojunction (SHJ) solar cells, with the layer stack shown in Fig. 4a. It was provided by Zhejiang AIKO Solar Technology Co., Ltd., and it features a front-side micro-texture with randomly distributed pyramids averaging 600–800 nm in height, and rear-side texture of 700–800 nm. The silicon bottom cell was laser-scribed with dimensions of 20 mm × 20 mm before using for perovskite-silicon tandem solar cells fabrication. 15 nm ITO recombination layer was served as the intermediate recombination layer. The wide bandgap perovskite top cell was deposited onto the silicon substrates. The perovskite processing details were the same as the single junction devices fabrication. Then 40 nm IZO was deposited by radio frequency magnetron sputtering at room temperature using a IZO target (In:Zn = 9:1), processed at 60 W and 3 mtorr in pure Argon. Silver (800 nm) at the rate of 4.0 Å s^{-1} was thermally evaporated through a designed mask as metal grid and the Ag electrode (800 nm) on the back of the silicon bottom cell was also deposited using this process. Finally, 100 nm MgF_2 as an antireflective layer was thermally evaporated at the rate of 2.0 Å s^{-1}.

Characterization of perovskite layers

The XRD and GIXRD patterns of perovskite films were characterized on a D8 ADVANCE system (Bruker Nano) using Cu Kα radiation (λ = 1.5418 Å). Perovskite films were prepared under the SAM covered substrates. XPS was performed on a Thermo Scientific ESCALab 250Xi using 200 W monochromated Al Kα (1486.6 eV) radiation. A 500 µm X-ray spot was used for XPS analysis. The base pressure in the analysis chamber was about 3×10^{-10} mbar. The SEM images and EDS mapping was acquired using a field-emission SEM (FEI NanoSEM650). SEM uses an electron beam accelerated at 500 V to 30 kV, enabling operation at a variety of currents. An accelerating voltage of 10 kV was used throughout EDS measurement, the spectrum were acquired from a series of maps (10 × 10 μm^2) on each sample. PL spectra were measured by a FLS1000 spectrometer. The excitation wavelength was set at 475 nm. TRPL spectra were measured by F900 spectrometer with a 375 nm pulsed laser (EPL-375). Two half device structures were used: Glass/FTO/SAM/Perovskite and Glass/Perovskite/Modification layer/C_{60}. The decay curves were fitted by the bi-exponential equation:

$$\phi(t) = t_0 + A_1 e^{-t/\tau_1} + A_2 e^{-t/\tau_2} \quad (1)$$

$$\tau_{\text{average}} = \frac{A_1\tau_1^2 + A_2\tau_2^2}{A_1\tau_1 + A_2\tau_2} \quad (2)$$

where $\phi(t)$ is the time-dependent PL photon flux, τ_1 represents the fast decay lifetime corresponding to carrier extraction process and τ_2 represents the slow decay lifetime relating to radiative recombination process. Based on TRPL results, we used the differential lifetime $\tau_{PL}(t)$ to have further analysis, it defined as the inverse negative slope of the logarithmically plotted PL photon flux $\phi(t)$:

$$\tau_{PL}(t) = -\left(\frac{dIn(\phi(t))}{dt}\right)^{-1} \quad (3)$$

In-situ PL for monitoring perovskite growth in initial stage was carried out by capturing the PL signal every 10 ms using Portman portable Raman spectrometer (PR532-T) produced by Ocean Optics. In-situ time-dependent PL tracking for perovskite film stability comparison was measured under white LEDs (about 2-sun light intensity). The PL spectra were scanned and recorded every ten minutes.

Device characterizations

J–*V* characteristics of WBG single-junction PSCs were recorded by a Keithley 2400 Source Meter and under a solar simulator from EnliTech (SS-X50R); a KG-5 Si photodiode was used to calibrate the solar simulator light intensity to 1-sun. The photovoltaic cells were measured both in reverse scan (1.32 V → 0 V, step 0.02 V) and forward scan (0 V → 1.32 V, step 0.02 V) in a nitrogen glovebox, under room temperature. For dark *I*–*V* measurement, the voltage continuously sweeps from −1.0 to 1.5 V with a step of 0.01 V, using a Keithley 6482 Source

Meter. *J*–*V* characteristics of perovskite/Si tandem solar cells were recorded by a Keithley 2450 Source Meter and under a solar simulator from EnliTech (SS-PST220R); a KG-3, and BL-7 silicon photodiode was used to synergistically calibrate the solar simulator light intensity to 1-sun. The tandem devices were measured both in reverse scan (2.04 V → 0 V, step 0.02 V) and forward scan (0 V → 2.04 V, step 0.02 V) in a nitrogen glovebox, under room temperature. Stabilized power output (SPO) results were performed under maximum power point (MPP) by fixing the cell at the MPP voltage (determined by the *J*–*V* scan in both scan directions) and tracking the changes of current over time, under room temperature. The device EQE was measured by EnliTech EQE measurement system (QE-R3018). Standard silicon and germanium solar cell were used as the references for the EQE measurement. For the tandem device measurement, bias illumination was used that the perovskite top cell was measured under an 850 nm continuous biased light and the silicon bottom cell was measured under a 470 nm continuous biased light. For the light-intensity-dependent *J*–*V* measurements, the data was analyzed with the formula:

$$V_{OC} = \frac{nkT}{q} \ln(I) + V'_{OC} \quad (4)$$

where n is the ideality factor, k is the Boltzmann constant, T is the temperature, q presents the unit charge, I presents the light intensity, and V'_{OC} is the constant.

Device stability measurements

The testing system was supported by Wuhan 91PVKSolar Technology Co. Ltd, China. The illumination was provided by a LED-based solar simulator, calibrated to approximately 1-sun intensity, the light spectrum was shown in Supplementary Fig. 20. For the encapsulated single-junction devices, the devices were put into a tightly closed chamber and N_2 flow was maintained during the testing. Throughout the operational tracking duration, a hot plate served as the thermal source to maintain the chamber temperature at approximately 65 °C, a temperature sensor was put into the chamber to monitor the temperature. SPO was monitored by applying a constant bias voltage of 800 mV to the single-junction device. The 85 °C thermal stability was carried out by putting unencapsulated device onto a hotplate with 85 °C, and cooled down to room temperature before *J*–*V* measurements. In the case of silicon/perovskite tandem device stability measurements, the devices were encapsulated in a nitrogen-purged glovebox using a desiccant impregnated polyisobutylene (PIB) edge seal between two glass sheets, the package method was similar as previously reported[59]. The packaged tandem devices were put onto a 65 °C hotplate to maintain the temperature and a bias voltage as 1500 mV was used for the tracking.

Reporting summary

Further information on research design is available in the Nature Portfolio Reporting Summary linked to this article.

Data availability

The data that support the findings of this study are available from the corresponding author upon request.

References

1. Tiedje, T., Yablonovitch, E., Cody, G. D. & Brooks, B. G. Limiting efficiency of silicon solar cells. *IEEE Trans. Electron Devices* **31**, 711–716 (1984).
2. National Renewable Energy Laboratory, Best Research-Cell Efficiency Chart. https://www.nrel.gov/pv/cell-efficiency.html (2025).
3. Bai, Y. et al. Initializing film homogeneity to retard phase segregation for stable perovskite solar cells. *Science* **378**, 747–754 (2022).
4. Liu, J. et al. Perovskite/silicon tandem solar cells with bilayer interface passivation. *Nature* **635**, 596–603 (2024).
5. Wang, Z., Song, Z., Yan, Y., Liu, S. & Yang, D. Perovskite—a perfect top cell for tandem devices to break the S–Q Limit. *Adv. Sci.* **6**, 1801704 (2019).
6. Chin, X. Y. et al. Interface passivation for 31.25%-efficient perovskite/silicon tandem solar cells. *Science* **381**, 59–63 (2023).
7. Mariotti, S. et al. Interface engineering for high-performance, triple-halide perovskite–silicon tandem solar cells. *Science* **381**, 63–69 (2023).
8. Ugur, E. et al. Enhanced cation interaction in perovskites for efficient tandem solar cells with silicon. *Science* **385**, 533–538 (2024).
9. Jiang, Q. & Zhu, K. Rapid advances enabling high-performance inverted perovskite solar cells. *Nat. Rev. Mater.* **9**, 399–419 (2024).
10. Zhang, J. et al. Minimizing tin (II) oxidation using ethylhydrazine oxalate for high-performance all-perovskite tandem solar cells. *J. Semicond.* **46**, 052802 (2025).
11. Aydin, E. et al. Interplay between temperature and bandgap energies on the outdoor performance of perovskite/silicon tandem solar cells. *Nat. Energy* **5**, 851–859 (2020).
12. Slotcavage, D. J., Karunadasa, H. I. & McGehee, M. D. Light-induced phase segregation in halide-perovskite absorbers. *ACS Energy Lett.* **1**, 1199–1205 (2016).
13. Knight, A. J. & Herz, L. M. Preventing phase segregation in mixed-halide perovskites: a perspective. *Energy Environ. Sci.* **13**, 2024–2046 (2020).
14. Motti, S. G. et al. Phase segregation in mixed-halide perovskites affects charge-carrier dynamics while preserving mobility. *Nat. Commun.* **12**, 6955 (2021).
15. Liang, Z. et al. Homogenizing out-of-plane cation composition in perovskite solar cells. *Nature* **624**, 557–563 (2023).
16. Jiang, Q. et al. Compositional texture engineering for highly stable wide-bandgap perovskite solar cells. *Science* **378**, 1295–1300 (2022).
17. Liu, J. et al. Efficient and stable perovskite-silicon tandem solar cells through contact displacement by MgFx. *Science* **377**, 302–306 (2022).
18. Xu, J. et al. Triple-halide wide–band gap perovskites with suppressed phase segregation for efficient tandems. *Science* **367**, 1097–1104 (2020).
19. Chen, Y. et al. Nuclei engineering for even halide distribution in stable perovskite/silicon tandem solar cells. *Science* **385**, 554–560 (2024).
20. Pei, F., Chen, Q. & Jiang, Y. Stability of wide-bandgap perovskites for tandem applications: a review. *Energy Mater. Adv.* **6**, 0172 (2025).
21. Li, Q. et al. Wide-bandgap subcells for all-perovskite tandem solar cells: recent advances, challenges, and future perspectives. *Energies* **18**, 2415 (2025).
22. Hu, Y. et al. Understanding the role of cesium and rubidium additives in perovskite solar cells: trap states, charge transport, and recombination. *Adv. Energy Mater.* **8**, 1703057 (2018).
23. Turren-Cruz, S.-H. et al. Enhanced charge carrier mobility and lifetime suppress hysteresis and improve efficiency in planar perovskite solar cells. *Energy Environ. Sci.* **11**, 78–86 (2018).
24. Erodici, M. P. et al. Enhanced charge carrier lifetime and mobility as a result of Rb and Cs incorporation in hybrid perovskite. *Appl. Phys. Lett.* **118**, 063901 (2021).
25. Ramadan, A. J., Oliver, R. D. J., Johnston, M. B. & Snaith, H. J. Methylammonium-free wide-bandgap metal halide perovskites for tandem photovoltaics. *Nat. Rev. Mater.* **8**, 822–838 (2023).
26. Wang, Z. et al. Suppressed phase segregation for triple-junction perovskite solar cells. *Nature* **618**, 74–79 (2023).
27. Wang, Z. et al. Regulation of wide bandgap perovskite by rubidium thiocyanate for efficient silicon/perovskite tandem solar cells. *Adv. Mater.* **36**, 2407681 (2024).

28. Li, F. et al. Highly efficient monolithic perovskite/perovskite/silicon triple-junction solar cells. *Adv. Mater.* **36**, 2311595 (2024).
29. Li, X. et al. Strain regulation of mixed-halide perovskites enables high-performance wide-bandgap photovoltaics. *Adv. Mater.* **36**, 2401103 (2024).
30. Park, Y. H. et al. Inorganic rubidium cation as an enhancer for photovoltaic performance and moisture stability of $HC(NH_2)_2PbI_3$ perovskite solar cells. *Adv. Funct. Mater.* **27**, 1605988 (2017).
31. Saliba, M. et al. Incorporation of rubidium cations into perovskite solar cells improves photovoltaic performance. *Science* **354**, 206–209 (2016).
32. Zhang, M. et al. High-efficiency rubidium-incorporated perovskite solar cells by gas quenching. *ACS Energy Lett.* **2**, 438–444 (2017).
33. Zheng, L. et al. Strain-induced rubidium incorporation into wide-bandgap perovskites reduces photovoltage loss. *Science* **388**, 88–95 (2025).
34. Yang, Y. et al. Amidination of ligands for chemical and field-effect passivation stabilizes perovskite solar cells. *Science* **386**, 898–902 (2024).
35. Yang, F. et al. Melamine hydroiodide functionalized $MAPbI_3$ perovskite with enhanced photovoltaic performance and stability in ambient atmosphere. *Sol. RRL* **3**, 1800275 (2019).
36. Kim, S.-G., Chen, J., Seo, J.-Y., Kang, D.-H. & Park, N.-G. Rear-surface passivation by melaminium iodide additive for stable and hysteresis-less perovskite solar cells. *ACS Appl. Mater. Interfaces* **10**, 25372–25383 (2018).
37. Luo, S. et al. Melamine holding PbI_2 with three "arms": an effective chelation strategy to control the lead iodide to perovskite conversion for inverted perovskite solar cells. *Energy Environ. Sci.* **18**, 2436–2451 (2025).
38. Lim, D.-H., Ramasamy, P., Kwak, D.-H. & Lee, J.-S. Solution-phase synthesis of rubidium lead iodide orthorhombic perovskite nanowires. *Nanotechnology* **28**, 255601 (2017).
39. Jung, M.-H., Rhim, S. H. & Moon, D. $TiO_2/RbPbI_3$ halide perovskite solar cells. *Sol. Energy Mater. Sol. Cells* **172**, 44–54 (2017).
40. Tang, B. et al. An all-inorganic perovskite-phase rubidium lead bromide nanolaser. *Angew. Chem. Int. Ed.* **58**, 16134–16140 (2019).
41. Chen, S. et al. Crystallization in one-step solution deposition of perovskite films: Upward or downward? *Sci. Adv.* **7**, eabb2412 (2021).
42. McMeekin, D. P. et al. A mixed-cation lead mixed-halide perovskite absorber for tandem solar cells. *Science* **351**, 151–155 (2016).
43. Song, T.-B. et al. Dynamics of antisolvent processed hybrid metal halide perovskites studied by in situ photoluminescence and its influence on optoelectronic properties. *ACS Appl. Energy Mater.* **3**, 2386–2393 (2020).
44. Li, F. et al. Hydrogen-bond-bridged intermediate for perovskite solar cells with enhanced efficiency and stability. *Nat. Photon.* **17**, 478–484 (2023).
45. Krogmeier, B., Staub, F., Grabowski, D., Rau, U. & Kirchartz, T. Quantitative analysis of the transient photoluminescence of $CH_3NH_3PbI_3/PC_{61}BM$ heterojunctions by numerical simulations. *Sustain. Energy Fuels* **2**, 1027–1034 (2018).
46. Kirchartz, T., Márquez, J. A., Stolterfoht, M. & Unold, T. Photoluminescence-based characterization of halide perovskites for photovoltaics. *Adv. Energy Mater.* **10**, 1904134 (2020).
47. Oliver, R. D. J. et al. Understanding and suppressing non-radiative losses in methylammonium-free wide-bandgap perovskite solar cells. *Energy Environ. Sci.* **15**, 714–726 (2022).
48. Chen, H. et al. Improved charge extraction in inverted perovskite solar cells with dual-site-binding ligands. *Science* **384**, 189–193 (2024).
49. Hartnagel, P. & Kirchartz, T. Understanding the light-intensity dependence of the short-circuit current of organic solar cells. *Adv. Theory Simul.* **3**, 2000116 (2020).
50. Wang, R. et al. Improving the efficiency and stability of perovskite solar cells using π-conjugated aromatic additives with differing hydrophobicities. *Energy Environ. Sci.* **16**, 2646–2657 (2023).
51. Tress, W. et al. Interpretation and evolution of open-circuit voltage, recombination, ideality factor and subgap defect states during reversible light-soaking and irreversible degradation of perovskite solar cells. *Energy Environ. Sci.* **11**, 151–165 (2018).
52. Caprioglio, P. et al. On the origin of the ideality factor in perovskite solar cells. *Adv. Energy Mater.* **10**, 2000502 (2020).
53. Luo, D., Su, R., Zhang, W., Gong, Q. & Zhu, R. Minimizing non-radiative recombination losses in perovskite solar cells. *Nat. Rev. Mater.* **5**, 44–60 (2020).
54. Tress, W. et al. Predicting the open-circuit voltage of $CH_3NH_3PbI_3$ perovskite solar cells using electroluminescence and photovoltaic quantum efficiency spectra: the role of radiative and non-radiative recombination. *Adv. Energy Mater.* **5**, 1400812 (2015).
55. Li, C. et al. Reducing saturation-current density to realize high-efficiency low-bandgap mixed tin–lead halide perovskite solar cells. *Adv. Energy Mater.* **9**, 1803135 (2019).
56. Proctor, C. M. & Nguyen, T.-Q. Effect of leakage current and shunt resistance on the light intensity dependence of organic solar cells. *Appl. Phys. Lett.* **106**, 083301 (2015).
57. Boccard, M. & Ballif, C. Influence of the subcell properties on the fill factor of two-terminal perovskite–silicon tandem solar cells. *ACS Energy Lett.* **5**, 1077–1082 (2020).
58. Köhnen, E. et al. Highly efficient monolithic perovskite silicon tandem solar cells: analyzing the influence of current mismatch on device performance. *Sustain. Energy Fuels* **3**, 1995–2005 (2019).
59. Jiang, Q. et al. Towards linking lab and field lifetimes of perovskite solar cells. *Nature* **623**, 313–318 (2023).

Acknowledgements

This work was financially supported by National Natural Science Foundation of China (grant No. 62374162, Q.J.), Beijing Natural Science Foundation (grant No.Z240024, Q.J.), CAS Project for Young Scientists in Basic Research (grant YSBR-090, J.Y. and Q.J.), National Key R&D Program of China (grant No. 2023YFB4204501, Q.J.), Guiding Funds of Central Government for Supporting the Development of the Local Science and Technology (grant No. 2024ZY0016, Q.J.), Space Application System of China Manned Space Program (CMSS-2024-4-B-006, X.Z.) and Xiamen Fengyi Optoelectronic Technology Co., LTD. We thank Zhejiang AIKO Solar Technology Co., Ltd and Dr. Kaifu Qiu and their support from Key Research and Development Program of Zhejiang Province (Grant No. 2024C01092, K.Q.). Y. Z. thanks the financial support from the National Natural Science Foundation of China (Grant No. 62522404 and 12421005, Y. Z.) and the Science & Technology Department of Hunan Province (Grant No. 2024JJ2041, Y. Z.).

Author contributions

Q.J. and Z.H. conceived the idea and designed the experiments. Q.J. and J.Y supervised the project. Z.H. fabricated single junction and tandem solar cells, worked on device stability test and analysis. Z.W. assisted with device fabrication, characterization and measurement results analysis. Z.X. performed DFT calculation under supervision of X.Z., J. Yang., and Y. L. performed TA characterization and analysis under supervision of Y.Z. Q.J. and Z.H. wrote the paper. T.L., S.Z., and L.W. all participated in the discussion and analysis on the paper.

Competing interests

The authors declare no competing interests.

Additional information

Supplementary information The online version contains supplementary material available at https://doi.org/10.1038/s41467-025-66480-7.

Correspondence and requests for materials should be addressed to Qi Jiang or Jingbi You.

Peer review information *Nature Communications* thanks the anonymous, reviewer(s) for their contribution to the peer review of this work. A peer review file is available.